Research Article | Vol. 28, No. 24 / 23 November 2020 / Optics Express 36219

Optics EXPRESS

Chromaticity of structural color in polymer thin film photonic crystals

GISELLE ROSETTA,[1] TONG AN,[2] QIBIN ZHAO,[2] JEREMY J. BAUMBERG,[3] JOHN J. TOMES,[1] MATT D. GUNN,[1] AND CHRIS E. FINLAYSON[1,*]

[1]Department of Physics, Prifysgol Aberystwyth University, SY23 3BZ, UK
[2]School of Materials Science and Engineering, Shanghai Jiao Tong University, Shanghai, 200240, China
[3]Cavendish Laboratory, University of Cambridge, CB3 0HE, UK
[*]cef2@aber.ac.uk

Abstract: A three-dimensional goniometric study of thin-film polymer photonic crystals investigates how the chromaticity of structural color is correlated to structural ordering. Characterization of chromaticity and the angular properties of structural color are presented in terms of CIE 1931 color spaces. We examine the viewing angle dependency of the Bragg scattering cone relative to sample symmetry planes, and our results demonstrate how increased ordering influences angular scattering width and anisotropy. Understanding how the properties of structural color can be quantified and manipulated has significant implications for the manufacture of functional photonic crystals in sensors, smart fabrics, coatings, and other optical device applications.

1. Introduction

Structural coloration arises from Bragg resonances within photonic crystals (PCs); wavelength-scale arrays described by a periodic refractive index contrast [1,2]. This iridescence is prevalent throughout nature, appearing in beetles [3], butterflies [4], and botany [5]. As a consequence of Bragg diffraction, the visual appearance of structural color is strongly dependent on both viewing and incident angles. The quantitative measurement [6] and modelling [7,8] of the optical properties of photonic crystals is vital such that engineering towards applications may be realized. There is a wide body of literature concerning scatterometry and reflectometry of biological photonic crystals [9–12] - however, there are comparatively few studies pertaining to synthetic structures, and fewer still that consider how changes in crystalline ordering affect the characteristic metrics of structural coloration. Our study seeks to address this gap in literature.

We report on the iridescence of 'polymer opals' (POs); viscoelastic films melt-shear ordered from core-shell nanoparticles. This is achieved with a technique known as Bending-Induced Oscillatory Shear (BIOS), whereby laminated thin films are drawn over heated rollers. hcp ordering has been shown to permeate these films with additional shearing. [13] Within these structures, coloration originates from the marginal index contrast $\Delta n \sim 0.1$ between the core and shell. Disruptions to, and imperfections in, lattice quality are known to result in the angular broadening of the structural color 'scattering cones' [14,15], however, this has never been fully quantified.

In this study, consideration of structural color in terms of the Commission Internationale de l'Eclairage (CIE) 1931 color space leads to a standardized representation of hue and chromaticity, allowing for a full quantification of color changes. Our results indicate how hue and saturation vary with increased microstructural ordering, as determined by transmission electron microscopy (TEM), as well as viewing angle and sample orientation relative to illumination. Structural order is shown to correlate with the angular width of the Bragg scattering cone, which we examine for multiple azimuthal planes relative to the shear ordering direction.

#410338 https://doi.org/10.1364/OE.410338
Journal © 2020 Received 17 Sep 2020; revised 16 Oct 2020; accepted 18 Oct 2020; published 13 Nov 2020

Optics EXPRESS

Structural coloration is central to the application of PCs in colorimetric sensing [16]. POs are particularly notable within this remit on account of their (reversible) stretch-tunability, which has previously been engineered to exhibit mechano-chromism, fluorescence quenching and other such novel optical properties [17,18]. PCs with coloration in the visible regime are candidates as anti-forgery devices in currency and merchandise, and there is growing interest in viscoelastic POs due to their mechanical robustness and compatibility with readily scalable roll-to-roll fabrication methods [13,19]. Our methodology and analysis are therefore highly relevant to the engineering and application of structural color.

2. Experimental methods

2.1. Fabrication and ordering characterization

The polymer opals in this study were fabricated from ~230nm diameter core-shell particles, constituting polystyrene (PS) cores with polyethyl acrylate (PEA) shells, grafted by a polymethyl methacrylate (PMMA) interlayer [Fig. 1(a)]. These nanoparticles were synthesized by a multi-stage emulsion polymerization with a volume ratio of 34:16:50 PS:PMMA:PEA, as previously reported [20]. The dried nanoparticles are melt-extruded into homogenous ribbons using a twin co-rotating screw mini-extruder at 150°C, and then press-laminated between two polyethylene terephthalate (PET) sheets of 100μm thickness. These PET-PO-PET sandwich structures were sheared over rollers of ~1cm diameter heated to 120°C, inducing shear strains of 300% at a rate of $1.5s^{-1}$. This bespoke rheological technique [Fig. 1(b)] is known as 'Bending Induced Oscillatory Shear' (BIOS) [13], facilitating a route to reproducible large-area roll-to-roll processing, with considerably improved tolerance to particle polydispersity as compared to colloidal methods [21].

Particle ordering begins at the outer edges of the film and permeates the bulk with successive shearing, resulting in random hexagonal close-packing (hcp) with the [111] plane presenting at the film surface [13,22,23]. The lattice displays some preferential particle alignment relative to the direction of shear; the associated direction vector $\hat{\mathbf{g}}$ is defined and illustrated in Figs. 1(b) and 1(c). Removal of the PET lamina results in free standing, permanently ordered polymer thin films of approximately 80-100μm thickness and typical areas of 5-10 cm^2 [Fig. 1(c)], with a net core-shell refractive index contrast of $\Delta n \approx 0.10$ - 0.12. Structural equilibrium occurs at around 40 cycles of BIOS [13], after which competing dissipative processes (such as shear-melting) tend to preclude any further incremental improvement in the ordering. A detailed description of the mechanisms of this process are outside the scope of this report and earlier reports can be found in Ref. [13]. We examine polymer opals with 0, 5, 10, 20, and 40 such cycles to determine the key order dependencies in terms of the saturation and angular distribution of structural color.

TEM was performed (Thermo Scientific Talos L120C G2, 120kV Montage Mode) to examine the depth of ordering within each sample [Fig. 1(d)]. The films were microtomed into 60-80μm slices using a diamond knife (Leica EM UC7&FC7) at -60°C. The ultrathin slices were placed on copper grids and stained with RuO_4 vapor for contrast enhancement. Images have been post-processed to enhance brightness, contrast, and sharpen image features. The original high-resolution TEM images are supplied as Visualization 1, Visualization 2, Visualization 3, Visualization 4 (0-, 5-, 20-, and 40-BIOS cycles respectively). A Bragg penetration depth for POs of ~10μm at normal incidence was estimated using a quasi-1D transfer matrix simulation (Fig. S1), with this skin-depth layer applied to subsequent analyses. The variation of effective refractive index (n_{eff}) with depth from the film surfaces was extracted for each film by an image analysis algorithm, and the refractive index contrast Δn_{eff} was inferred in each case (see Table 1). The TEM images illustrate clear evidence of layering in the well-ordered regions of the films, and Fourier transform methods (Lomb Periodogram variant) were applied to determine the corresponding spatial frequency *F*. It is strongly evident from both the real-space periodicity in the micrographs, and the derived spatial frequency spectra with Gaussian broadening parameter

Optics EXPRESS

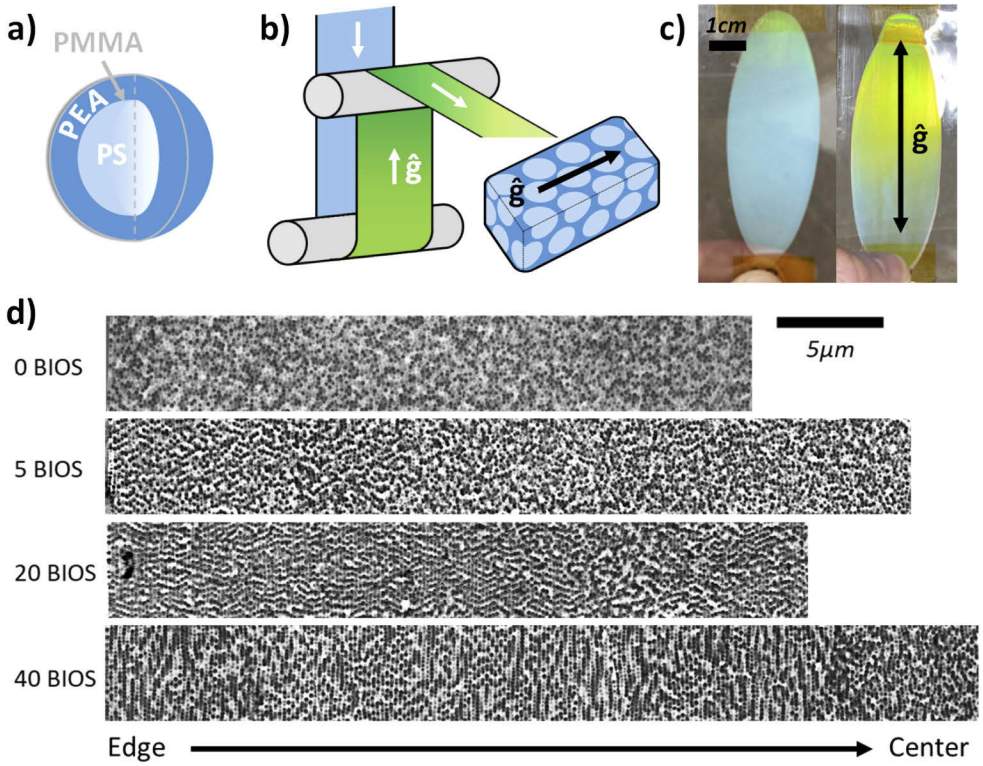

Fig. 1. a) Polymer opal (PO) core-shell nanoparticle with three distinct layers; b) simplified schematic of BIOS, where encapsulated polymer films are drawn over heated rollers to induce order; c) comparison of pre-shear and BIOS ordered POs, with an arrow indicating the processing direction of BIOS $\hat{\mathbf{g}}$; d) TEM imaging (contrast enhanced) of the PO cross-section for 0-40 BIOS passes, demonstrating how the superficial ordering at 0 BIOS can be significantly improved up to 40 BIOS passes - at which ordering has fully permeated the now monolithic film.

ΔF (full width at half maximum), that BIOS processing results in the sequential permeation of increased structural ordering. Treating this "sharpness" of the distribution in spatial frequencies as an order parameter of the surface regions, this improvement is readily illustrated by the significant decrease in ΔF going from 0 up to 20 BIOS cycles, with the ratio ΔF/F decreasing markedly from 0.048 to 0.021.

Table 1. Ordering characterization of the 10μm skin depth BIOS POs in terms of depth ordering (as estimated from TEM images), spatial frequency F and ΔF as determined from Fourier analyses, and Δn_{eff}.

Number of BIOS passes	Approx. ordering depth (μm) ±0.25	F (μm^{-1}) ±0.2	ΔF (μm^{-1}) ±0.005	Δn_{eff} ±0.0005
0	0.75	5.2	0.25	0.022
5	8.75	5.9	0.24	0.036
20	22.5	5.3	0.11	0.052
40	38.0	5.2	0.21	0.046

Optics EXPRESS

2.2. Goniometric reflectance measurement and CIE mapping

Despite the extensive prior structural and sampling depth characterization that has been undertaken by Zhao et al. [13], information regarding the effect of ordering and structural anisotropy on the reflectance properties of POs remains incomplete. We apply goniophotometry (REFLET 180S) to measure three-dimensional reflectance and scattering within select azimuthal planes φ_m in terms of viewing angle θ_m. This is in combination with the simultaneous measurement of individual wavelength scattering intensities across the visible spectrum.

POs were aligned in one of two orientations, with the BIOS processing direction lying either parallel or perpendicular to the plane of incidence; these configurations are denoted by the symbols $\parallel$ and $\perp$ respectively. A halogen tungsten bulb of color temperature 3200K was incident on the films at $\theta_I = 15°$, 30°, 45°, and 60° from the azimuth, with a collimated incident spot of diameter ≈ 8mm. Scattered light was collected by a fiber-coupled CCD spectrophotometer with detector solid angle $\pm 3.4 \times 10^{-4}$ Sr. Measurements were taken with 0.1° and 1nm resolution as a function of viewing angle θ_m and wavelength respectively. Detection and sample apparatus [Fig. 2(a)] were situated within a dark-box environment. Reflectance was calibrated with reference to a Spectralon Lambertian standard scatterer and dark background spectrum.

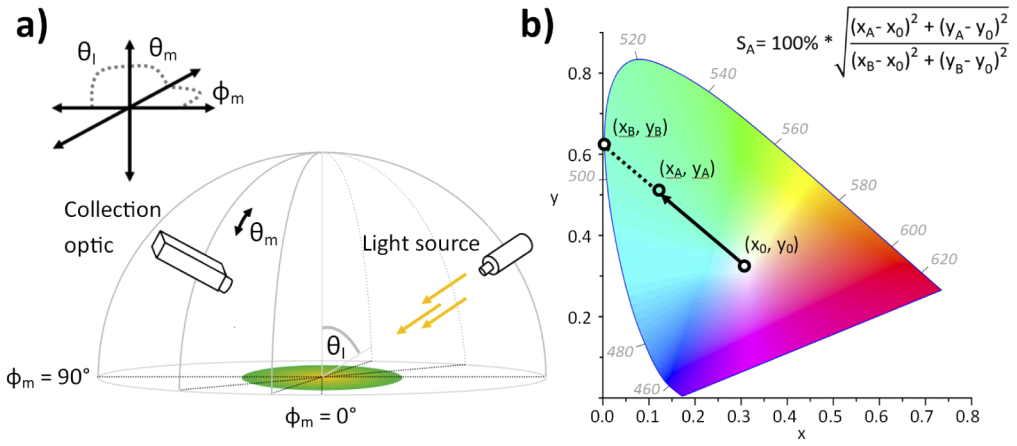

Fig. 2. a) Reflectometry setup with sample alignment and spherical co-ordinate nomenclature indicated; b) CIE 1931 color space rendered with Origin, illustrating the saturation percentage calculation (equation inset) by mapping a linear function through A and the white point to intercept the line of monochromes at point B.

A scattering cone matrix is compiled, I_z (λ,θ_m), with a z-axis of relative reflectance. The maximum intensities at each viewing angle, I_{max} (θ_m), and the corresponding wavelengths, I_{max} (λ_{peak}), can be numerically extracted. Voigt profiles are subsequently fitted to I_{max} (θ_m) in order to ascertain the angular range (FWHM) of structural color, $\Delta\theta_m = \theta_m^+ - \theta_m^-$, and corresponding wavelength tuning range, $\Delta\lambda = \lambda_{peak}(\theta_m^+) - \lambda_{peak}(\theta_m^-)$. From I_z (λ, θ_m) the chromaticity co-ordinates *x* and *y* are obtained [24]. Finally, these values are cross-referenced with the angular tuning ranges obtained from the Voigt profiles and measured color spectra within the range $\Delta\theta_m$ only are mapped onto the CIE 1931 color space.

We quantify saturation for point A (x_A, y_A) in the color space in terms of 'excitation purity' [25]; a percentage of the distance from A towards the outer gamut boundary from the white point $x_0 = y_0 = 1/3$, whereby a linear function through both points intersects the gamut boundary (line of monochromes) at point B (x_B, y_B) [Fig. 2(b)]. Average saturation is reported by taking the average of the point saturation values over the range $\Delta\theta_m$, with appropriate correction for both obscuration and specular reflection. Characteristic hue is reported in terms of the 'dominant

Optics EXPRESS

wavelength' corresponding to the point B. Linear interpolation of the gamut geometry introduces a small error in hue and saturation estimated as ±0.5%.

3. Results and discussion

As an important benchmark, an opal film without BIOS processing was first examined [Fig. 1(c), left]; as shown from TEM, this structure lacks any long-range crystalline ordering. Coloration is primarily caused by diffusive non-resonant scattering [26], with residual milky-blue color arising from the average plane spacing (correlation length) [27]. As expected, this coloration shows little angular dependence, and can be represented on the color space by minimal displacement from the white point [Fig. 3(a), '0']. This gives a low average saturation of 4%, and a dominant wavelength of ~490 nm, as corroborated by visual appearance.

As order is progressively introduced into these nanoparticle arrays, the resonant scattering feature around 550 nm grows markedly as shown for 5 and 40 BIOS [Figs. 3(b)–3(d)]; a commensurate improvement in color saturation is observed. Additionally, a noticeable red-shift occurs in this feature, as is consistent with the changes in spatial frequency evident from the TEM analysis; i.e. a decreasing spatial frequency corresponds to a greater spatial periodicity between particle planes, and thus longer wavelength optical resonances. Angular and spectral tuning can be observed for 5 BIOS cycles in Fig. 3(c), with this culminating in a bright scattering cone at 40 BIOS shown in Fig. 3(d). With only 10 cycles of BIOS processing, color purity in each measured azimuthal plane φ_m across the scattering cone reaches a maximum of 45-50% when the BIOS direction $\hat{\mathbf{g}}$ lies in the plane of light incidence (Table 2). This represents a significant increase in saturation to that seen for the 0 BIOS film. However, when the plane of incidence is set perpendicular to $\hat{\mathbf{g}}$, the saturation is only seen to increase to around 30%. A similar result is seen in all azimuthal (φ_m) planes when illumination is perpendicular to $\hat{\mathbf{g}}$, where color saturation is consistently lower (Table 2). This result demonstrates that light is scattered over a larger range of wavelengths, and at a lower intensity, when the plane of illumination is perpendicular to the BIOS direction, as compared to when it is parallel to $\hat{\mathbf{g}}$. This observation of anisotropy in scattering response provides further evidence of sphere 'chaining' defects within the crystal, which have been both predicted and directly observed, [22,28,29] reinforcing observations that ordering in BIOS preferentially occurs in the direction of shear. Of additional note here is the persistence of the low intensity short-wavelength scattering, even after application of the BIOS process; this is readily evident if the scattering cone data are compared on the same dynamic scale (Fig. S2). This differentiation between resonant and non-resonant scattering mechanisms merits further investigation and modelling, particularly as the latter unexpectedly begins to exhibit some degree of directionality at 40 BIOS cycles. Given the clear and demonstrable effect of structural ordering and anisotropy on the optical properties of polymer opals, simulation modelling of analogues using computational tools is indeed an interesting and challenging ongoing project, following on from the more rudimentary optical models we utilize in the current paper (Fig. S1).

Color saturation is seen to plateau at 10 cycles because progressive depth-ordering induced by subsequent BIOS develops to depths beyond λ_{Bragg} (~10 μm at normal incidence) associated with backscattering. This is corroborated by our TEM observations (Fig. 2) and our transfer matrix simulation model, as set out in the Fig. S1. However, as also consistent previous reports [13], this zone of greatest ordering becomes situated somewhat beneath the surface layer as BIOS progresses beyond 20 up to 40 cycles. As a commensurate reversal of the trend of decreasing ΔF values in Table 1, the FWHM of spatial frequency is seen to increase, strongly indicative of some reduction of the optimized ordering within the sampled top 10-micron region, thus effecting a depreciation in the scattering saturation metrics. Hence, as light is primarily diffracted by the outermost layers of the structure, the effects on saturation of the increased structural order also become less significant. Further results confirming these trends are shown in Table S1.

Optics EXPRESS

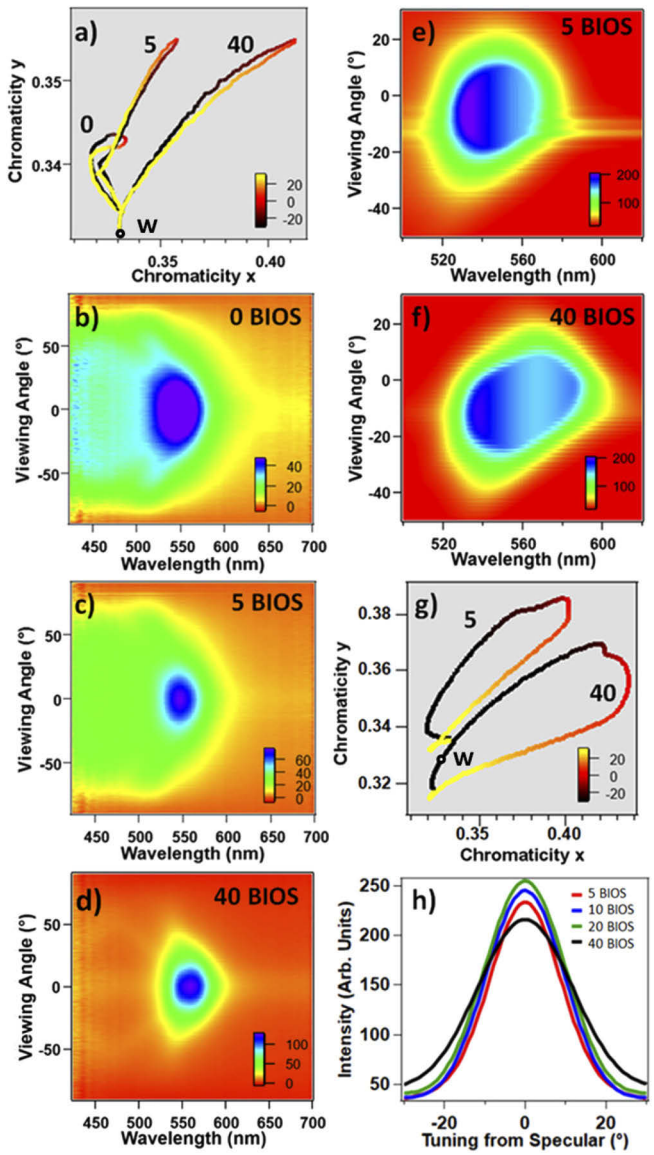

Fig. 3. a) CIE color space projection, with the white point denoted by **w**, of structural colour for 0, 5, and 40 BIOS passes with detuning of θ_m from specular direction (°) indicated by the color scaling, as derived from the scattering cone responsivities of b) 0-, c) 5-, and d) 40-BIOS respectively, whereby $\theta_I = 15°$ parallel to $\hat{\mathbf{g}}$, viewed perpendicular to the plane of incidence ($\varphi_m = 0°$). Scattering cones are plotted for e) 5-BIOS and f) 40-BIOS POs ($\varphi_m = 60°$, $\theta_I = 15°$ perpendicular to $\hat{\mathbf{g}}$ using the same relative reflectance scaling, with resultant CIE space trajectories shown in g). In h), a Voigt function is fitted to the locus of maximum intensity (at λ_{peak} for each spectrum) as a function of θ_m, and the Voigt full-width half maximum extracted, such that angular broadening as a function of BIOS can be quantified.

Optics EXPRESS

Table 2. The average saturation of reflected color in the $\varphi_m = 60°$ azimuthal plane for polymer opals of varying BIOS cycles ($\theta_I = 15°$, incident both perpendicular ($\perp$) and parallel ($\parallel$) to $\hat{g}$), and the corresponding angular widths ($\Delta\theta_m$) for the structural color scattering cone.

Number of BIOS cycles	Average saturation (%) ±0.5		Difference (%) ±0.7	Angular width of scattering cone (°)		Difference (%)
	Plane of incidence ‖ to BIOS	Plane of incidence ⊥to BIOS		Plane of incidence ‖ to BIOS	Plane of incidence ⊥ to BIOS	
5	32	33	1	23 ± 5	36 ± 11	57
10	47	44	3	23 ± 4	32 ± 9	39
20	41	39	2	23 ± 5	30 ± 8	30
40	38	40	1	28 ± 6	36 ± 12	29

However, the resultant hue, scattering intensity, and angular distribution of the scattering cone are seen to tune with increased order past 10 BIOS cycles. This can be illustrated by comparing Figs. 3(e)–3(g), where the scattering cone demonstrates spectral broadening, implying that subsequent processing continues to affect the global ordering in the sample - in agreement with microscopy observations as well as the values of spatial frequency and Δn_{eff} shown in Table 1. Such results (summarized in Table 3 and Tables S2 corroborate existing spatio-temporal understanding of the monotonic BIOS process, where there are a range of counteracting shear-induced ordering and disordering processes occurring simultaneously [13,30].

Table 3. Structural color tuning ranges ($\Delta\lambda$) and dominant wavelengths of reflected color for polymer opals of varying BIOS cycles ($\theta_I = 15°$), observed in the plane of incidence. A tuning range is not reported for 0-BIOS as no scattering cone is measurable. Measurements are compared for sample orientations with the BIOS direction vector $\hat{g}$ being either parallel or perpendicular to the plane of incidence.

Number of BIOS cycles	Plane of incidence ‖ to BIOS		Plane of incidence ⊥ to BIOS	
	Tuning range (nm) ±1	Dominant wavelength (nm) ±2.5	Tuning range (nm) ±1	Dominant wavelength (nm) ±2.5
0	-	494	-	495
5	562–509	578	533 - 590	583
10	572 - 604	580	544 - 590	591
20	572 - 593	582	549 - 604	586
40	576 - 613	585	561 - 616	594

Table 2 furthermore illustrates the angular broadening of the scattering cone in terms of viewing angle θ_m, and this effect is present in all azimuthal (φ_m) planes. Angular broadening with increasing BIOS cycles is further evident from Fig. 3(h), where beyond 20 cycles we also observe a decrease in measured maximum intensity as light scattering broadens both spectrally and in term of angular cone width. Whilst some variance in data is noted, in particular with respect to positional variations, these observational trends are also strongly corroborated by recently reported reflectometry data on comparable "red opal" samples [31].

This data can be vividly represented as loci that track across the CIE color space [Figs. 4(a) and 4(b)], as θ_m is varied, forming characteristic trajectories. The diagrams are indicative of disordered opals being of a light blue hue, gaining a green-yellow appearance at 5-10 BIOS, and then a more yellow-orange appearance at 20-40 BIOS cycles. This tuning of structural color with increased ordering towards longer wavelengths can be attributed to an incremental change in the [111] layer-spacing normal to the sample plane [13,23] rather than any changes

Optics EXPRESS

to the in-plane ordering. In terms of the corresponding hue values [Fig. 4(a)] it is seen that there is tuning of the reflectance towards the shorter wavelengths across all azimuthal planes, demonstrating the expected accordance with the Bragg-Snell law. However, less expected is the angle of incidence dependence on the average structural color saturation, which was observed to significantly decrease from 45% to approximately 30% when θ_I was increased from 30° to 45°, as shown in Table 4 and Fig. 4(c). Again, our simulations of Bragg length indicate that λ_{Bragg} decreases markedly as θ_I shifts away from normal incidence towards oblique angles, which will reduce the total optical path of light within the ordered structure, and we attribute this as the likely mechanism for this effect.

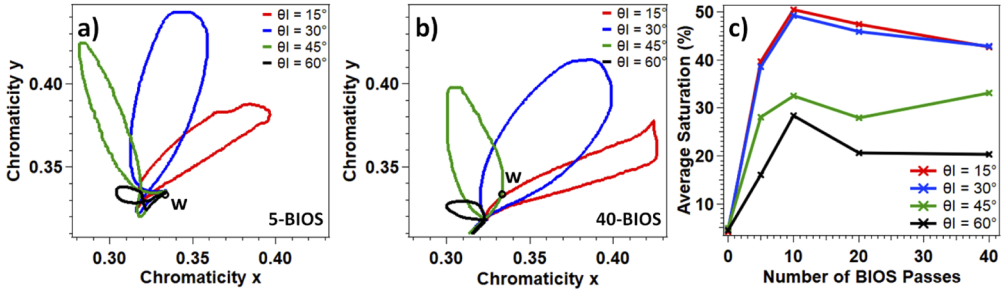

Fig. 4. CIE color space loci, as derived from scattering cone data as θ_m is varied, forming characteristic trajectory shapes, with the white point denoted by w. Data is shown for the $\varphi_m = 60°$ azimuthal plane for a) 5-BIOS and b) 40-BIOS, with light incident parallel to $\hat{\mathbf{g}}$; c) average saturation of structural color across the scattering cones for differing incident angle across a range of BIOS passes, demonstrating both the plateau in saturation appearing at 10-BIOS and how saturation decreases with increasing θ_I from the zenith.

Table 4. Average saturation (±0.5%), observed in the plane of incidence $\varphi_m = \pm 90°$ for varying θ_I, demonstrating how saturation decreases as the incidence angle is displaced from the azimuth. Measurements are compared for sample orientations with the BIOS direction vector $\hat{\mathbf{g}}$ being parallel or perpendicular to the plane of light incidence. Data is shown for samples of 0-40 BIOS cycles as indicated.

θ_I (°)	Plane of incidence ∥ to BIOS					Plane of incidence ⊥ to BIOS				
	0	5	10	20	40	0	5	10	20	40
15	4	40	50	47	43	3	40	51	49	48
30	5	39	49	46	43	3	37	45	40	45
45	5	28	32	28	33	3	29	36	33	37
60	4	16	28	21	20	3	23	16	30	26

4. Conclusion

In summary, we have developed techniques to both characterize and elucidate the chromaticity properties of structural color from high-quality polymer opal films, using direct TEM imaging of shear-ordered structures as cross-reference. As a key advance on earlier reports, these techniques were successfully applied in conjunction with adapted colorimetry models to quantify a number of key structural coloration metrics; developments which will readily be of a more general applicability to the study of ordered structurally colored systems. The application of shear-induced ordering and associated iterative improvements in structural order, correlates directly with very large quantitative increases, of at least an order of magnitude, in the angle-specific color saturation. Increased ordering also leads to spectral broadening of the scattering cone over a range

Optics EXPRESS

of wavelengths dependent on incident and viewing angle. We thus gain an improved knowledge of these archetypal thin-film photonic crystals, as a key analogue to many structurally-colored systems, and how shear-inducing ordering correlates with scattering cone characteristics and chromaticity metrics. This provides the groundwork for further imaging and quantitative color mapping of scattering cones in three dimensions, with direct impact on the feasibility and design of structurally colored materials in a wide array of potential applications, from anti-forgery to aesthetic and design. Further computational modelling of polymer opals, extending towards detailed optical bandgap and dispersion analysis, would provide even greater insight into the scattering hemispheres of these materials, in terms of both reflectivity and transmission. This is vital for a deeper intuition of how opaline thin films manufactured from the cyclical BIOS process can be engineered effectively for use as optical devices.

Funding

Llywodraeth Cymru (KESS-2 (European Social Fund), SPARC-II (European Regional Development Fund)); National Natural Science Foundation of China (No. 51903155); Natural Science Foundation of Shanghai (No. 19ZR1474700).

Acknowledgements

The authors thank the Deutsches Kunststoff-Institut (DKI), Germany and Varichem Co. Ltd, UK for supply and development of materials, the UCL Colour & Vision Research Laboratory for access to CIE tabulations, Dr. Anita Brady-Boyd for assistance in image rendering, and Malvern Panalytical Ltd for access to equipment.

Disclosures

The authors declare no conflicts of interest.

See Supplement 1 for supporting content.

Data availability

https://10.20391/a97740d2-bb68-45fe-af1d-3e10e424804e

References

1. E. Yablonovitch, "Inhibited Spontaneous Emission in Solid-State Physics and Electronics," Phys. Rev. Lett. **58**(20), 2059–2062 (1987).
2. J. V. Sanders, "Colour of Precious Opal," Nature **204**(4964), 1151–1153 (1964).
3. A. E. Seago, P. Brady, J. Vigneron, and T. D. Schultz, "Gold bugs and beyond: a review of iridescence and structural colour mechanisms in beetles (Coleoptera)," J. R. Soc. Interface **6**(suppl_2), S165–S184 (2009).
4. S. Kinoshita, S. Yoshioka, Y. Fujii, and N. Okamoto, "Photophysics of structural color in the Morpho butterflies," Forma **17**, 103–121 (2002).
5. S. Vignolini, E. Moyroud, B. J. Glover, and U. Steiner, "Analysing photonic structures in plants," J. R. Soc. Interface **10**(87), 20130394 (2013).
6. S. Kinoshita, S. Yoshioka, and J. Miyazaki, "Physics of structural colors," Rep. Prog. Phys. **71**(7), 076401 (2008).
7. A. Mekis, J. C. Chen, I. Kurland, S. Fan, P. R. Villeneuve, and J. D. Joannopoulos, "High Transmission through Sharp Bends in Photonic Crystal Waveguides," Phys. Rev. Lett. **77**(18), 3787–3790 (1996).
8. M. Ahles, T. Ruhl, G. P. Hellmann, H. Winkler, R. Schmechel, and H. von Seggern, "Spectroscopic ellipsometry on opaline photonic crystals," Opt. Commun. **246**(1-3), 1–7 (2005).
9. D. G. Stavenga, H. L. Leertouwer, P. Pirih, and M. F. Wehling, "Imaging scatterometry of butterfly wing scales," Opt. Exp. **17**(1), 193–202 (2009).
10. T. A. Harvey, K. S. Bostwick, and S. Marschner, "Directional reflectance and milli-scale feather morphology of the African Emerald Cuckoo, *Chrysococcyx cupreus*," J. R. Soc. Interface **10**(86), 20130391 (2013).

Optics EXPRESS

11. E. van Hooijdonk, C. Barthou, J. P. Vigneron, and S. Berthier, "Angular dependence of structural fluorescent emission from the scales of the male butterfly Troïdes magellanus (Papilionidae)," J. Opt. Sci. B **29**(5), 1104–1111 (2012).
12. P. Vukusic and D. G. Stavenga, "Physical methods for investigating structural colours in biological systems," J. R. Soc. Interface **6**, S133–S148 (2009).
13. Q. Zhao, C. E. Finlayson, D. R. E. Snoswell, A. Haines, C. Schäfer, P. Spahn, G. P. Hellmann, A. V. Petukhov, L. Herrmann, P. Burdet, P. A. Midgley, S. Butler, M. Mackley, Q. Guo, and J. J. Baumberg, "Large-scale ordering of nanoparticles using viscoelastic shear processing," Nat. Commun. **7**(1), 11661 (2016).
14. C. E. Finlayson and J. J. Baumberg, "Polymer opals as novel photonic materials," Polymer Int. **62**(10), 1403–1407 (2013).
15. C. E. Finlayson, A. I. Haines, D. R. E. Snoswell, A. Kontogeorgos, S. Vignolini, J. J. Baumberg, P. Spahn, and G. P. Hellmann, "Interplay of index contrast with periodicity in polymer photonic crystals," Appl. Phys. Lett. **99**(26), 261913 (2011).
16. S. Kim, A. N. Mitropoulos, J. D. Spitzberg, H. Tao, D. L. Kaplan, and F. G. Omenetto, "Silk inverse opals," Nat. Photonics **6**(12), 818–823 (2012).
17. O. L. J. Pursiainen, J. J. Baumberg, K. Ryan, J. Bauer, H. Winkler, B. Viel, and T. Ruhl, "Compact strain-sensitive flexible photonic crystals for sensors," Appl. Phys. Lett. **87**(10), 2003–2006 (2005).
18. C. G. Schäfer, M. Gallei, J. T. Zahn, J. Engelhardt, G. P. Hellmann, and M. Rehahn, "Reversible Light-, Thermo-, and Mechano-Responsive Elastomeric Polymer Opals Films," Chem. Mater. **25**(11), 2309–2318 (2013).
19. X. Shen, P. Wu, C. G. Schäfer, J. Guo, and C. Wang, "Ultrafast assembly of nanoparticles to form smart polymeric photonic crystal films: a new platform for quick detection of solution compositons," Nanoscale **11**(3), 1253–1261 (2019).
20. T. Ruhl, P. Spahn, and G. P. Hellman, "Artificial opals prepared by melt compression," Polymer **44**(25), 7625–7634 (2003).
21. Q. Zhao, C. E. Finlayson, C. G. Schaefer, P. Spahn, M. Gallei, L. Hermann, A. V. Petukhov, and J. J. Baumberg, "Nanoassembly of Polydisperse Photonic Crystals Based on Binary and Ternary Polymer Opal Alloys," Adv. Opt. Mater. **4**(10), 1494–1500 (2016).
22. C. E. Finlayson and J. J. Baumberg, "Generating Bulk-Scale Ordered Optical Materials Using Shear-Assembly in Viscoelastic Media," Materials **10**(7), 688 (2017).
23. C. E. Finlayson, P. Spahn, D. R. E. Snoswell, G. Yates, A. Kontogeorgos, A. I. Haines, P. Hellmann, and J. J. Baumberg, "3D Bulk Ordering in Macroscopic Solid Opaline Films by Edge-Induced Rotational Shearing," Adv. Mater. **23**(13), 1540–1544 (2011).
24. CIE Technical Report, Colorimetry 4th ed. (CIE, 2018).
25. V. R. Shrestha, S. Lee, S. Kim, and D. Choi, "Non-iridescent Transmissive Structural Color Filter Featuring Highly Efficient Transmission and High Excitation Purity," Sci. Rep. **4**(1), 4921 (2015).
26. L. Schertel, L. Siedentop, J. Meijer, P. Keim, C. M. Aegerter, G. J. Aubry, and G. Maret, "The Structural Colors of Photonic Glasses," Adv. Opt. Mat. **7**(15), 1900442 (2019).
27. P. M. Ossi, *Disordered Materials*, 2nd ed. (Springer, 2006).
28. J. J. Baumberg, O. L. Pursiainen, and P. Spahn, "Resonant optical scattering in nanoparticle-doped polymer photonic crystals," Phys. Rev. B **80**(20), 201103 (2009).
29. A. I. Haines, C. E. Finlayson, D. R. E. Snoswell, P. Spahn, G. P. Hellmann, and J. J. Baumberg, "Anisotropic Resonant Scattering from Polymer Photonic Crystals," Adv. Opt. Mater. **24**(44), OP305–OP308 (2012).
30. D. R. E. Snoswell, C. E. Finlayson, Q. Zhao, and J. J. Baumberg, "Real-time measurements of crystallization processes in viscoelastic polymeric photonic crystals," Phys. Rev. E. **92**, 052315 (2015).
31. G. Rosetta, M. Butters, J. J. Tomes, J. Little, M. D. Gunn, and C. E. Finlayson, "Quantifying the saturation of structural color from thin film polymeric photonic crystals," Proc. SPIE **11289**, 112890B (2020).